Physics and Technology of SPECT/CT

1

Dale L. Bailey and Kathy P. Willowson

1.1 SPECT/CT: Combining Form with Function

The introduction of combined SPECT (single photon emission computed tomography) and X-ray CT (computed tomography) scanners has changed the practice of single photon imaging in nuclear medicine forever. The original motivators to produce a combined SPECT/CT system were to provide improved anatomical localisation of the distribution of the SPECT radiopharmaceutical and to improve the capability of the SPECT scanner to produce images that can be corrected for the photon scattering and attenuation that cause degradation of the image.

The functional information contained in the SPECT images is complemented by the anatomical information (the 'form') provided by the CT scanner in numerous ways, including:

- Anatomical localisation of the SPECT radiopharmaceutical distribution.
- Correction for photon attenuation.
- Correcting for scattered radiation.
- Ability to determine the impact of the partial volume effect (PVE) due to the limited spatial resolution of the SPECT camera.
- The ability to calibrate the SPECT images in absolute units of radioactivity (kBq ml^{-1}).
- Introducing new clinical applications based on quantitative imaging in SPECT that require absolute radioactivity measures.
- The ability to convert the quantitative SPECT images into standardised uptake values (SUV).

This chapter will concentrate on the physics and technology relevant to combined SPECT and X-ray CT imaging.

1.2 The Development of Multimodality SPECT/CT Imaging

The first multimodal imaging performed with SPECT was developed to provide more accurate attenuation correction methods. In the 1980s, a number of groups were actively producing crude CT-like measurements on the gamma camera using radionuclide transmission sources such as Gadolinuiom-153 (Gd-153) [1–4]. The radionuclide sources were used to produce external photon beams with which the patient could be irradiated to produce a transmission image. The advantage of these measurements is that they could be performed on the gamma camera thus

D. L. Bailey (✉) · K. P. Willowson
Department of Nuclear Medicine, Royal North Shore Hospital, Sydney, NSW, Australia
e-mail: dale.bailey@sydney.edu.au; kathy.willowson@sydney.edu.au

H. Ahmadzadehfar et al. (eds.), *Clinical Applications of SPECT-CT*,
https://doi.org/10.1007/978-3-030-65850-2_1

obviating the need for a separate second detector. When a transmission radionuclide of different photon energy to the emission radionuclide's γ-ray energy was used, the emission and transmission measurements could be made simultaneously [1]. An example is shown in Fig. 1.1. For further discussion about these systems, the reader is referred to the review article by Bailey [5]. This technology found extensive use in SPECT myocardial perfusion imaging for correcting photon attenuation and has been incorporated into imaging guidelines issued by professional organisations [6].

However, even while these developments were being implemented others were starting to explore the use of CT with SPECT. Moore used a CT scan as the 'true' density distribution for attenuation correction in the early 1980s [7], and Fleming showed how a CT scan could be used in an iterative algorithm to produce quantitative SPECT reconstructions [8]. Hasegawa led a group in the early 1990s that sought to integrate many of these developments by producing a single detector that could record the X-rays from a CT source as well as the γ photons emitted by an in vivo radiopharmaceutical [9]. The

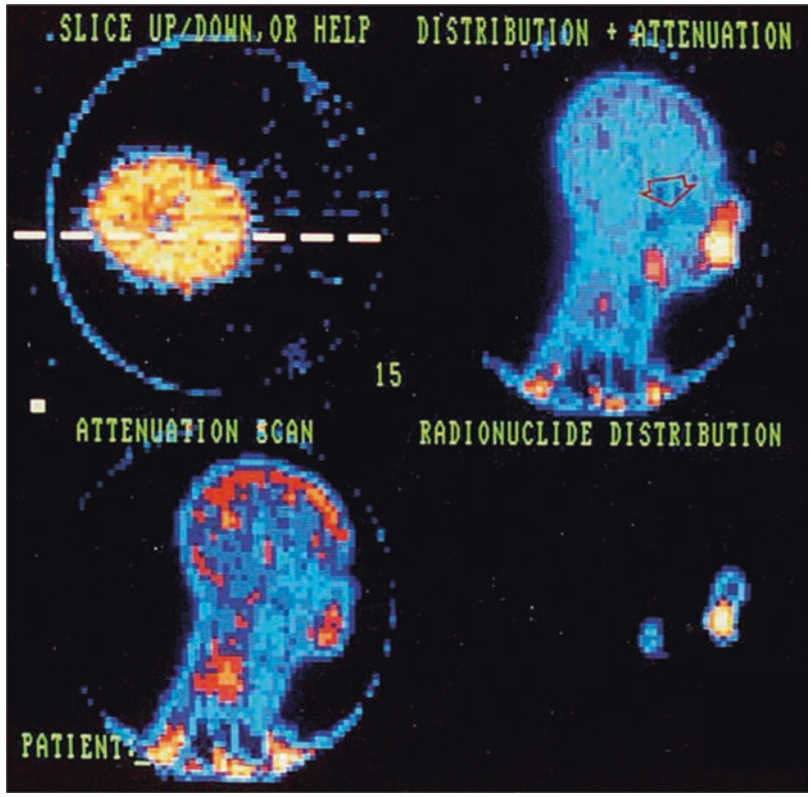

Fig. 1.1 An example from the mid-1980s of a simultaneous emission and transmission scan acquired with a gamma camera in a subject with a locally advanced cancer of the base of the tongue, intended for treatment with catheter-directed intra-arterial chemotherapy. The low resolution anatomical image is produced using a Gd-153 external radionuclide source. Gd-153 has two γ photons of energies 97 and 103 keV and thus is readily separated by pulse height discrimination from Tc-99 m (140 keV). The image shows an example of intra-arterially administered [^{99m}Tc]-MAA ("RADIONUCLIDE DISTRIBUTION" in lower right corner) and the reconstruction from the Gd-153 transmission source ("ATTENUATION SCAN" bottom left) in the sagittal plane. The fused image is shown in the top right corner and a reference image, a transaxial section, in top left corner. The red arrow on the fused image shows the approximate location of the tumour, indicating that the current location of the catheter needed to be revised for better tumour targeting. For further information, see Butler et al. [33]

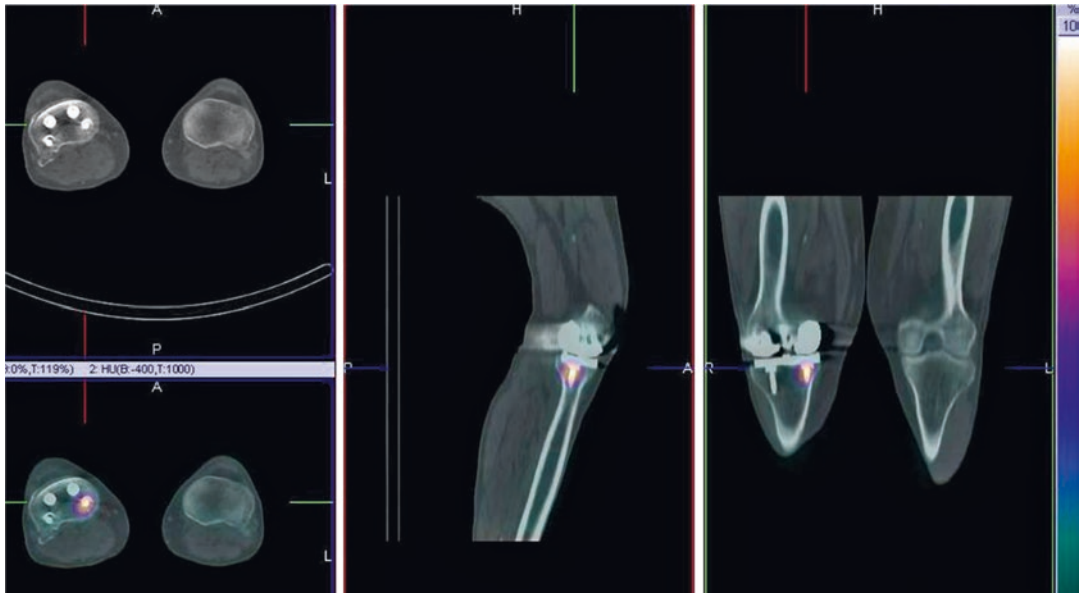

Fig. 1.2 An example from a contemporary SPECT/CT system demonstrating focally increased uptake on a ^{99m}Tc bone scan around an orthopaedic screw 3 years after knee replacement. The potential causes include infection, loosening or bony reaction to the screw

original detector was made from high-purity Germanium but they explored other detectors at a later stage [10]. In addition, the same group combined a diagnostic CT scanner with a conventional gamma camera [11] using standard detectors. The combined clinical scanners shared a common patient table for sequential SPECT and CT imaging. In the late 1990s, a combined gamma camera and X-ray CT system became commercially available based on a low beam current (1.0–2.5 mA) X-ray tube (GE Discovery VG Hawkeye) [12]. Having demonstrated the benefits of combined multi-modal SPECT/CT imaging on this platform, which was enormously successful commercially, other groups and vendors explored the added value of integrating a fully capable diagnostic CT scanner with dual-head SPECT gamma cameras (e.g., see [13]).

Today, combined SPECT and CT scanners are available in a variety of configurations with different CT scanner performance from flat panel detectors using cone-beam CT geometry, originally developed for on-board imaging on radiotherapy LINACs, to high-end conventional fast multi-detector (e.g., 2, 4, 6, 16, and 64 slice) systems. Figure 1.2 shows a recent clinical example from such a device.

1.3 Radiation and Interaction with Matter

The ability to produce cross-sectional images of the human body, whether using an external source of X-ray photons or from an internal source of γ photons, utilises radiation that can penetrate the body's tissues. Radiation can be divided into particulate radiation, such as alpha, beta and positron, or electromagnetic radiation, that is, mass-less quantised energy. Examples of different types of electromagnetic radiation that the reader would be more familiar with include radio waves, visible light, infrared radiation (heat), and microwaves as well as the high energy radiations which can cause ionisation of atoms such as X-rays, γ-rays, and cosmic (γ) radiation. Table 1.1 lists some properties of some of the ionising radiation encountered in nuclear medicine.

In general, nuclear medicine utilises γ radiation to form images with a gamma camera, annihilation radiation emitted after positron-electron

Table 1.1 Types of radiation and properties used in nuclear medicine imaging and therapy

Type of radiation	Symbol	Mass (kg)	Origin	Typical energy (MeV)
Alpha	α^{2+}	6.64×10^{-27}	Nucleus	>2
Beta	β^{-}	9.11×10^{-31}	Nucleus	0.2–4.0+
Positron	β^{+}	9.11×10^{-31}	Nucleus	0.2–4.0+
X-ray	X	0	Electron shells	0.04–0.10
Gamma	γ	0	Nucleus	0.05–0.5
Annihilation	γ±	0	Outside atom	0.511
Bremsstrahlung	–	0	Outside atom	0.2–4.0+
Auger	–	9.11×10^{-31}	Electron shells	<0.05

The radiations without mass are all electromagnetic

annihilation with a PET camera, X-rays to measure tissue density using a CT scanner, and alpha or beta radiation for radionuclide therapy. A further secondary form of radiation, Bremsstrahlung, is produced as an electron path deviates due to the influence of a nearby charged particle (usually the nucleus of an atom). From classical physics, we know that any force acting on a charged particle causing acceleration will result in radiation being produced. As an electron, in an X-ray tube or produced as a result of β^- decay, passes through matter, it will experience many deviations and collisions resulting in a continuous spectrum of radiation being emitted, the Bremsstrahlung, literally 'braking radiation' in German. Superimposed onto this continuous spectrum is the characteristic radiation emitted when electrons drop down from outer shells to fill the vacancies caused by ionisation, resulting in a polychromatic spectrum of energies (Fig. 1.3) as opposed to the monochromatic radiation seen with most γ-emitters used in nuclear medicine imaging.

Electromagnetic radiation interacts with matter by three principal mechanisms: the photoelectric effect, Compton scattering, and pair production. The photoelectric effect is the predominant mechanism by which X-rays interact with matter, and for the γ-ray energies used in nuclear medicine, the predominant mode of interaction is Compton scattering. This distinction has implications when using X-ray CT data in SPECT attenuation correction algorithms as the absorption profile is different.

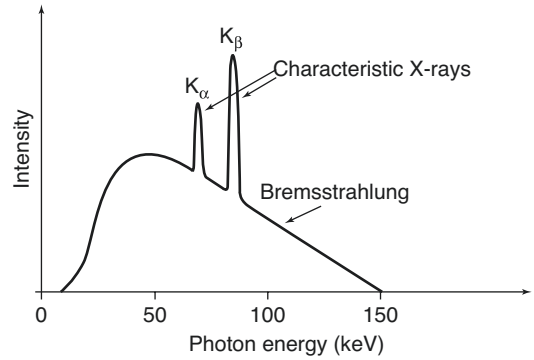

Fig. 1.3 A hypothetical X-ray spectrum is shown illustrating the polychromatic nature of the photons produced by the continuum of Bremstrahlung radiation superimposed with the characteristic radiation corresponding to different transitions within the electron shells

X-rays, being in general of lower photon energy than γ-rays, tend to be totally absorbed by the photoelectric interaction with inner shell orbital electrons in the tissues of the body. The higher energy γ-rays are more likely to interact with a weakly bound outer shell electron in a Compton interaction whereby they lose some energy in the elastic scattering and change direction. The two effects are illustrated in Fig. 1.4.

The energy of the scattered photon can be found from the Compton equation:

$$E_\gamma^{'} = \frac{E_\gamma}{1 + \frac{E_\gamma}{m_e c^2}\left[1 - \cos\left(\theta_C\right)\right]} \qquad (1.1)$$

where E_γ and $E_\gamma^{'}$ are the incident and scattered photon energies, respectively, m_e is the non-

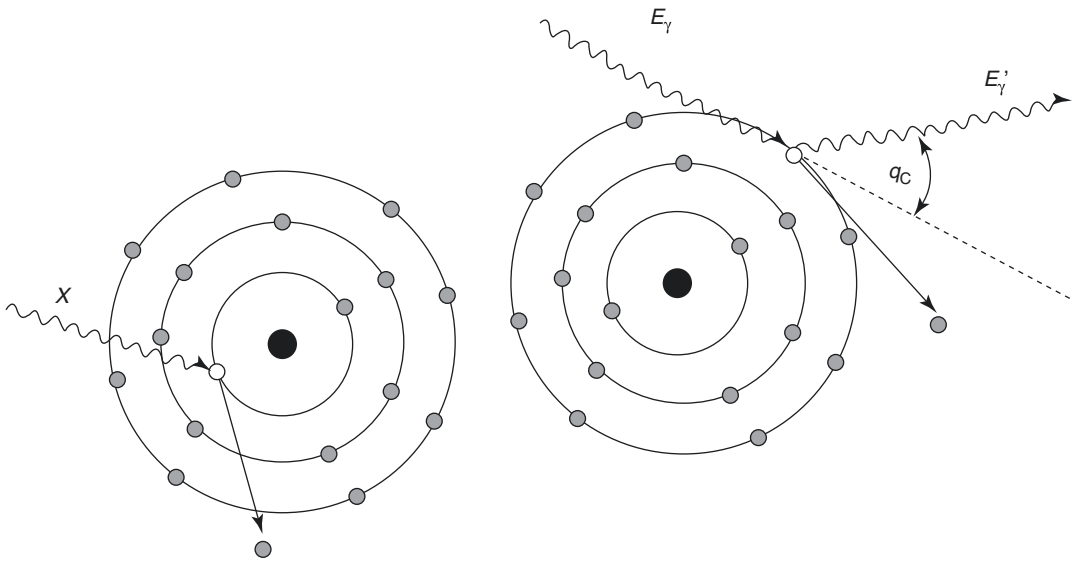

Fig. 1.4 The photoelectric effect (left) is where an incident photon (**X**) displaces an inner shell electron thereby leaving a vacancy and ionising the atom. X-rays and Auger electrons may be produced after as the vacancy is filled by an outer shell electron. Compton scattering (right) is more probable at higher photon energies. The incoming photon ($\mathbf{E}_\gamma$) elastically scatters off a weakly bound outer shell electron changing direction and resulting in a photon of slightly lower energy ($\mathbf{E}_\gamma'$)

relativistic rest mass of the electron, c is the speed of light ($m_e c^2$ = 0.511 MeV), and θ_C is the angle through which the photon has been scattered (the 'Compton angle').

1.3.1 Photon Attenuation

For a well-collimated source of photons and detector, attenuation takes the form of a mono-exponential function, i.e.,

$$I_x = I_0 \, e^{-\mu x} \tag{1.2}$$

where I represents the photon beam intensity, the subscripts '0' and 'x' refer, respectively, to the unattenuated beam intensity and the intensity measured through a thickness of material of thickness x, and μ refers to the attenuation coefficient of the material (units:cm^{-1}). Attenuation is a function of the photon energy and the electron density (Z number) of the attenuator. The attenuation coefficient is a measure of the probability that a photon will be attenuated by a unit length of the medium. The situation of a well-collimated source and detector is referred to as narrow-beam condition.

However, when dealing with in vivo imaging, we do not have a well-collimated source, but rather a source emitting photons in all directions equally. Under these uncollimated conditions, photons whose original emission direction would have taken them out of the acceptance angle of the detector may be scattered such that they are detected. This is known as 'broad-beam' conditions indicating increased acceptance of scattered photons leading to an overall lower effective attenuation coefficient (Fig. 1.5). A table of broad- and narrow-beam attenuation coefficients for radionuclides commonly used in nuclear medicine is given in Table 1.2. This distinction between the broad and narrow-beam cases is important when it comes to applying attenuation and scatter correction in SPECT reconstruction as it will have a large impact on the reconstructed data.

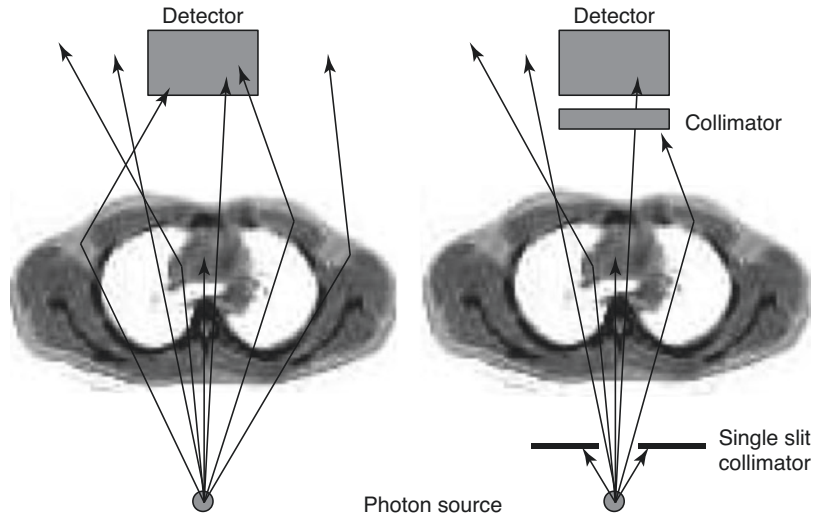

Fig. 1.5 An illustration of the difference between narrow-beam and broad-beam geometry is shown. In the broad-beam cause, more photons are detected compared to the narrow-beam situation so that the effect of attenuation appears to be lessened. When the source is internally distributed within the body and radiation is being given off in all directions, it is a broad-beam situation

Table 1.2 Attenuation Coefficients for commonly used single photon radionuclides in water

Radionuclide	Peak (keV)	NIST XCOM	Narrow beam (cm^{-1})	Broad beam (cm^{-1})
Tc-99 m	140	0.151	0.149	0.121
I-131	364	0.110	0.099	†
In-111	171	0.142	0.135	0.103
	245	0.127	0.121	0.104
Ga-67	93	0.169	0.171	0.153
	185	0.139	0.143	0.107
	300	0.118	0.123	0.099
I-123	159	0.137	0.138	0.114
Tl-201	75–80, 167	–	0.159, 0.137	0.123

These are values that we have compiled from a variety of sources. The NIST (US National Institute of Standards & Technology) XCOM values are available in an on-line resource (see: http://physics.nist.gov/PhysRefData/XrayMassCoef/ComTab/water.html accessed March 2013). The narrow and broad beam values have been measured on the gamma camera and are those used in our practice [18]. († – not measured to date)

1.4 SPECT Instrumentation

1.4.1 Gamma Camera

The workhorse imaging device for SPECT today remains the gamma camera (Fig. 1.6). New solid-state devices have been introduced clinically and will be discussed later. The gamma camera has remained virtually unchanged since its introduction by Anger in the late 1950s. It consists of an inorganic scintillator crystal, sodium iodide doped with small amounts of thallium (NaI(Tl)) to enhance light production, to which is coupled a close packed array of photomultiplier tubes (PMTs) which converts the light produced by the scintillator into an electrical signal. The electrical signal produced contains information about the location of the photons' interaction with the crystal plus pulse height spectroscopy (energy deposited in crystal) information.

The most common configuration for a SPECT camera today is a dual-detector device. This is because this configuration affords the most flexibility in general nuclear medicine imaging, permitting static planar imaging, moving bed whole-body planar scanning, and SPECT with the heads at various relative angles to each other, e.g., 90°, 120°, and 180°. While the gamma camera has retained the same basic design for over 50 years, refinements and improvements in the instrumentation, especially increased digitisation of the signals, have resulted in an extremely stable device suitable for rotation and translation without impacting on image quality.

As the γ-photons are emitted from the subject in all directions, a lead collimator is required between the scintillation crystal and the source to define the parallel lines of response that the photons have taken. The collimator has requirements such as high attenuation (lead is almost always used), thickness, hole shape, length and width to

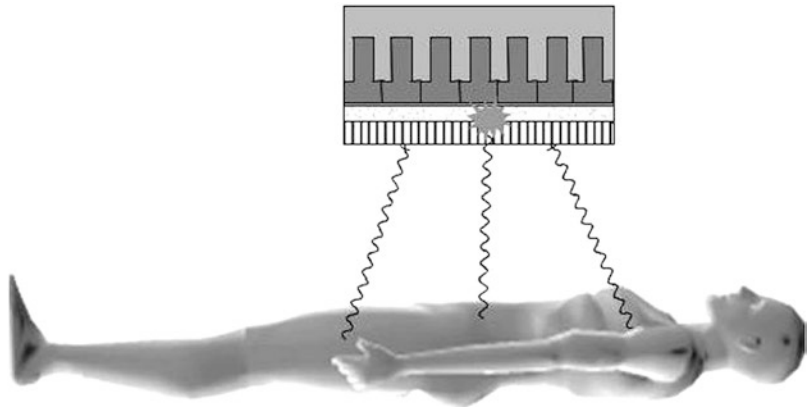

Fig. 1.6 Photons emitted from the subject travelling in a direction orthogonal to the detector pass through the holes of the collimator while the photons from other angles are attenuated. The photons emit a burst of light which is proportional in intensity to the energy absorbed in the crystal, which is then localised by the photomultiplier tube array

attenuate the photons that need to be excluded when imaging at a particular orientation to the subject. The resolution of the gamma camera is primarily limited by the geometric resolution of the collimator, which is of the order of 6–9 mm at a distance of 10 cm from the collimator. Overall resolution for the gamma camera is a function of a number of factors including the detector (intrinsic) and collimator (geometric) resolution, the distance from the emitting source to the collimator, the energy of the radionuclide, and the size and density of the object or body being imaged. The sensitivity of the gamma camera is primarily limited by the collimator. The absolute sensitivity in air for a typical gamma camera to a non-attenuating source of 140 keV γ-rays is around 100–200 detected events (counts) per second per MBq ($ct.s^{-1}{\cdot}MBq^{-1}$), or around 0.01–0.02% of all emitted events. The collimator is the component of the imaging chain which places the greatest restriction on gamma camera performance—it has very low sensitivity given the available photon flux and its geometry imposes limits on the spatial resolution achievable. To compound this, sensitivity and spatial resolution have to be traded against each other to achieve a compromise—high sensitivity giving poor spatial resolution and higher resolution coming with decreased sensitivity.

The energy resolution of the NaI(Tl) scintillator is limited to around 10% FWHM (Full Width at Half Maximum) in the range 0.1–1.0 MeV. This precludes discriminating against photons that have undergone a scattering interaction within the body from which they originate, with a concomitant loss of energy. The net effect is that around 20–50% of all events detected by the gamma camera have been scattered within the body, accompanied by a change of direction, which gives rise to mispositioning. This degrades image quality by contributing to an increased background level and therefore decreased contrast. It also confounds attempts to quantify the radionuclide distribution. It is for this reason that scatter correction methods are required for quantitative SPECT reconstructions.

1.4.2 Solid-State Detectors

Recently, dedicated organ-specific SPECT systems with fundamentally different designs to the gamma camera have been introduced. Rather than using a conventional scintillator crystal for photon detection, these new systems use solid-state detectors which are able to convert the absorbed energy from the photon directly into an electrical signal. Due to the cost of these detectors at present, they are being developed for very specific applications such as cardiac imaging. The design for the systems includes a large number of small detectors (~10–30) which are located

in a fixed position. These systems are SPECT-only devices not capable of forming planar images. Collimation is usually done using simple pinhole designs, and the reconstruction is tailored to the unique geometry of the system. Among the attractive features of these systems are high sensitivity due to the large number of detectors focused on a small field of view and improved energy resolution compared with NaI(Tl). The improved energy resolution presents the possibility of simultaneous imaging of different radionuclides with similar photon energies (e.g., ^{99m}Tc (140 keV) and ^{123}I (159 keV)). The systems can be used for more rapid image acquisition due to the improved sensitivity with reductions of 4–10-fold reported. Alternately, the improvement in sensitivity can be used to reduce the amount of radioactivity injected and hence reduce the radiation dose received by the subject.

1.5 SPECT Acquisition and Reconstruction

1.5.1 Projections and the Radon Transform

Tomographic imaging is the art of reconstructing the internal distribution of the signal of interest from external measurements. The same principles for image formation are employed in CT, SPECT, and PET as well as in other imaging modalities such as con-focal microscopy. High energy photons are used because of their ability to pass through the body with subsequent detection by an external device.

The tomographic imaging process for SPECT is shown in Fig. 1.7. Photons are emitted from the subject at all angles but the collimator on the gamma camera selects only those travelling in the required direction at a particular angle of the detector relative to the subject. As seen in the figure, each row on the detector is composed of a series of parallel projections. The projections are proportional to the sum of the intensities of the radionuclide concentration along the particular line of sight through the subject. This can be written (ignoring photon attenuation at present) as:

$$p\left(x_r,\phi\right)=\int_{-\infty}^{+\infty} f\left(x,y\right)dy_r \tag{1.3}$$

where $p(x_r, \phi)$ is the one-dimensional projection of the two-dimensional function $f(x,y)$ in a rotating frame of reference (indicated by the subscript 'r') at the angle ϕ. This is known as a Radon (or 'X-ray') transform—$p(x_r, \phi)$ is the Radon transform of $f(x,y)$ at angle ϕ. The reconstruction of $f(x,y)$ from the projections is known as an 'inverse problem'. Note that the dimensionality of the original function $f(x,y)$, 2D, is reduced by one in the projection to a 1D profile. However, if multiple 1D projections at different angles over 180° or 360° are acquired, rotating about the z-axis, the 2D function $f(x,y)$ can be recovered using the solution provided by the Central Slice Theorem. This relates the projections and the original distribution $f(x, y)$ as the Fourier transform of a projection $p(x_r, \phi)$ of a distribution $f(x, y)$ are equal to a section through the Fourier transform of the distribution $f(x, y)$ at the same angle (ϕ) as the projection. For a more detailed discussion of this important concept, the reader is referred to one of the following texts on the topic [14–16].

The SPECT reconstruction problem is complicated by the fact that there are extra terms which were ignored, for clarity, in Eq. (1.3). A more complete description of the projection $p(x_r, \phi)$ is shown below where there is an additional attenuation term in the integrand, and there are additive terms to account for scatter (S) and Poisson (random) noise (η).

$$p\left(x_r,\phi\right)=\int_{-\infty}^{+\infty} f\left(x,y\right)\cdot e^{\int_{-\infty}^{y}-\mu\left(x,y\right)}dy_r+S\left(x_r,\phi\right)+\eta \tag{1.4}$$

1.5.2 Image Reconstruction: Filtered Back-Projection (FBP)

The classical method for image reconstruction in emission tomography is the filtered back-projection algorithm (Fig. 1.8). The advantages of the filtered

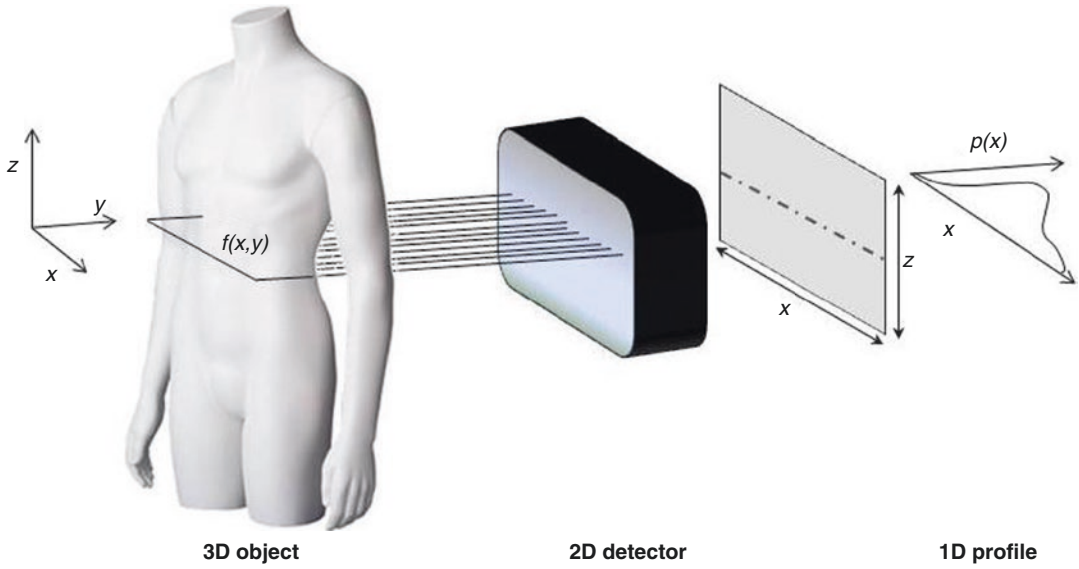

Fig. 1.7 The acquisition geometry is defined for SPECT acquisitions. The (x, y) co-ordinate system rotates about the z-axis to acquire projection ($p(x)$) at different angles. A section through the 3-dimensional radionuclide distribution in the subject ($f(x, y)$) is recorded by the detector as a 2D Radon transform. Each 1D profile in the planar image is then treated independently in the reconstruction process

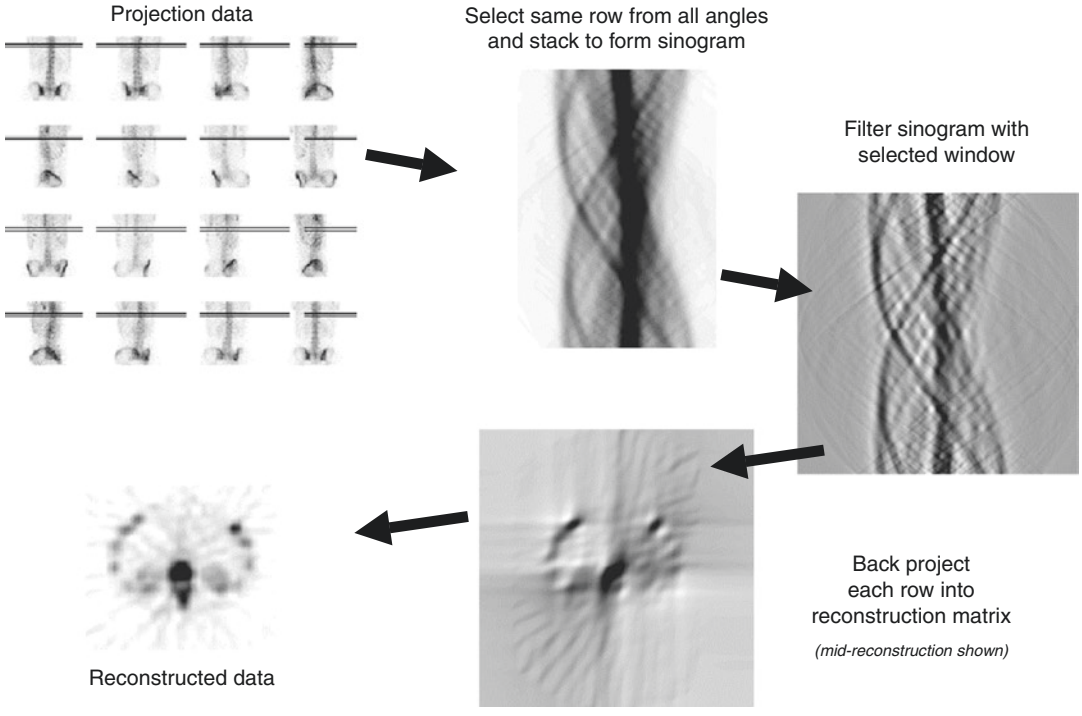

Fig. 1.8 The steps in reconstruction by filtered back-projection

back-projection approach are that it is computationally efficient and well-suited to optimisation using vector-based hardware (i.e., array processors). The alternative methods, such as iterative methods like Simultaneous Iterative Reconstruction Technique (SIRT), Algebraic Reconstruction Technique (ART), Iterative Least-Squares Techniques (ILST), or direct analytical methods (e.g., two-dimensional Fourier reconstruction), and statistical approaches (e.g., maximum-likelihood expectation-maximisation algorithm—ML-EM), are, in general, far more computationally expensive. In filtered back-projection, the projection data are firstly filtered, row by row (i.e., 1D filtering) and then back-projected. The pre-back-projection filtering is done to mitigate the blurring inherent in the back-projection operation.

Filtered back-projection was originally applied to reconstructing two-dimensional images from one-dimensional projection data recorded at many angles about the object in radioastronomy and electron microscopy. Back-projection involves projecting the acquired data back across the reconstruction matrix. At each angle, the detected events from each projection are evenly distributed between each element on the ray. After doing this from a large number of angles, the elements with the highest detected event rates will have the highest reconstructed intensity, but unfortunately elements that did not contain any signal also have an unwanted 'background' contribution from the blurring in back-projection.

In order to understand this process, we start with a simple object, a point source. The back-projected image of a point source from multiple angles has the appearance of a star. The distance between the lines of the star increases with increasing distance from the point source. If the distance from the point source is r, then the value of the final back-projected value is $1/r$. If there are a lot of projection angles, then it makes sense to say that the density of the lines in a region is proportional to $1/r$ (Fig. 1.9). All of these extra lines lead to a very blurred reconstruction. We consider that each point in the image acts independently of those around it, and so each produces a star-like pattern. The combined effect of all of these star artefacts is to produce a very blurred image of little use. However, this can be corrected by filtering the data, usually before back-projection. The filter which corrects for this blurring is called the ramp filter due to its shape (Fig. 1.10).

Conventional filtered back-projection has been the traditional choice for reconstructing the internal distribution of a radiopharmaceutical in

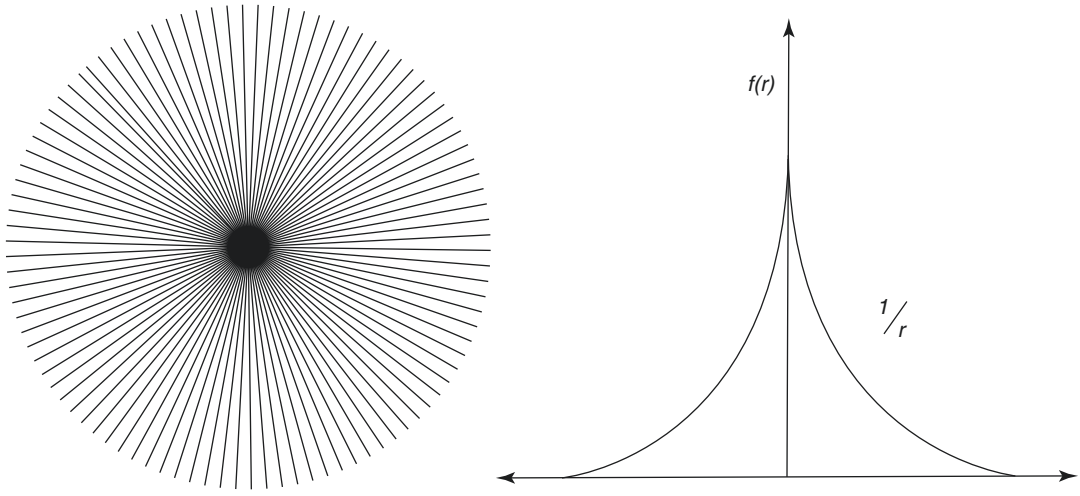

Fig. 1.9 Te 'star artefact' pattern seen on the left demonstrates the increase in density of the lines in simple back-projection that would be seen for a point source located at the centre of the matrix. The graph on the right shows diagrammatically how the density decreases rapidly at increasing radial distance from the origin

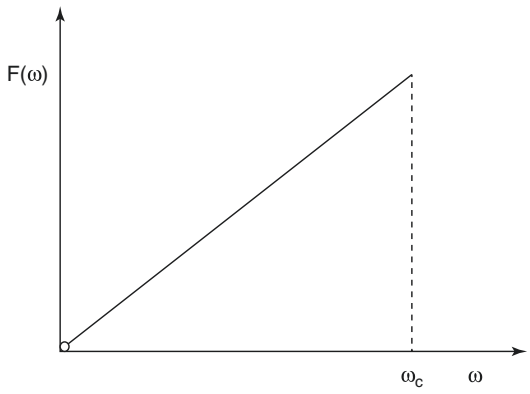

Fig. 1.10 Ramp filter in the Fourier (frequency) domain. The independent variable on the horizontal axis is the spatial frequency, ω, and the dependent variable on the vertical axis is the value that the function $F(\omega)$ takes for each value of ω. The ramp filter is truncated at a critical frequency, ω_c. The ramp filter corrects for the blurring in the back-projection process

emission tomography due to its speed. As for all radionuclide emission modalities, the recorded events for a particular line-of-response (LOR, one projection bin in a parallel acquisition geometry) consist of the integrated, *attenuated* contributions from all emission sources along the line-of-sight. Without applying any correction for attenuation, the contributions from locations deeper in the object will be relatively decreased due to attenuation compared with more peripheral emission origins. Filtered back-projection reconstruction does not handle this type of inconsistency well, as the relationship between attenuation and emission is inseparable. This is not the case in PET, where attenuation correction using measured transmission data is a simple and accurate correction. Correction for attenuation has been the major restriction on quantitative SPECT studies, to the point where SPECT was previously considered non-quantitative. Considerable progress on this topic has been made in recent years.

The disadvantages of filtered back-projection are:

- Due to the random nature of radioactive decay and the statistical uncertainties ('noise') that this introduces, plus attenuation and scattering, the projection data are *inconsistent* with respect to each other, and this causes artefacts in the reconstructed image if not corrected for prior to reconstruction.
- The filtering step before back-projection done to remove the blurring inherent in back-projection amplifies the high-frequency components of the projection data, and in doing so, greatly increases the statistical noise in the projections as this is a high frequency component of the data. Thus, filtered back-projection can be thought of as a noise-amplification process.
- It is not possible to build into the reconstruction process models of the data acquisition process which affect the final reconstruction, and which are well-understood and easily characterised, such as differences in resolution at different depths in the object, attenuation, and scattering. In this sense, filtered back-projection is a naïve approach to reconstructing an image from projection data.

1.5.3 Image Reconstruction: Iterative Techniques.

In recent years, the reconstruction algorithm of choice in emission tomography has moved from filtered back-projection to an approach based on one of the statistical iterative methods, with many applications using the block-iterative, Ordered Subset EM algorithm (OSEM) [17]. This approach has numerous attractive features including the ability to model physical characteristics of the acquisition process in the reconstruction in order to enhance image quality and accuracy and to better control the signal:noise ratio (SNR) of the final image. Most reconstruction software today includes optional scatter and attenuation correction and, increasingly, depth-dependent resolution recovery (referred to as PSF (point spread function) correction).

In an iterative reconstruction, an estimate of the original distribution $f(x,y)$ is formed based on the measured projection data. This estimate is then Radon transformed and compared with the acquired projection data, which is a Radon transform of the actual distribution $f(x, y)$.

Differences are determined, and a new estimate of $f(x, y)$ is produced. This is again Radon transformed and compared with the acquired projection data. This process is carried out a number of times with each iteration hopefully converging towards a closer match between the Radon transform of the current estimate of $f(x, y)$ and the acquired projection data. When the differences fall below a pre-determined threshold, the reconstruction is considered to have found a solution. A schematic diagram of the process is shown in Fig. 1.11.

1.5.4 Corrections for Photon Attenuation and Scattering

CT data from SPECT/CT can be used to correct for photon attenuation and scattering, usually in separate steps, after scaling the voxel values from CT (or Hounsfield) units to linear attenuation coefficients (μ) appropriate for the radionuclide that was used, as the energy of the X-ray photons and the γ photons will be different. It has been shown that the conversion from the CT numbers to the higher energy γ photon attenuation has a bi-linear relationship [18] (Fig. 1.12). The CT number is a relative number that is referenced to the attenuation of water in a calibration procedure. It is defined as:

$$CT_i = \mathrm{K}\frac{\mu_i - \mu_{\mathrm{water}}}{\mu_{\mathrm{water}}} \tag{1.5}$$

where i refers to the ith element of the data, and K is a scaling factor that accounts for the operating conditions of the CT scanner (tube voltage, *etc.*).

The implementation of this bi-linear scaling requires the CT image to be pre-processed into two distinct data sets—one data set containing the CT values below the pre-determined threshold value where the relationship changes, and the other above the threshold. In practice, this is easily achieved by segmenting the CT image on the basis of the CT values into two separate images, applying a different regression equation to each to scale to the appropriate values for the radionuclide being used, and then

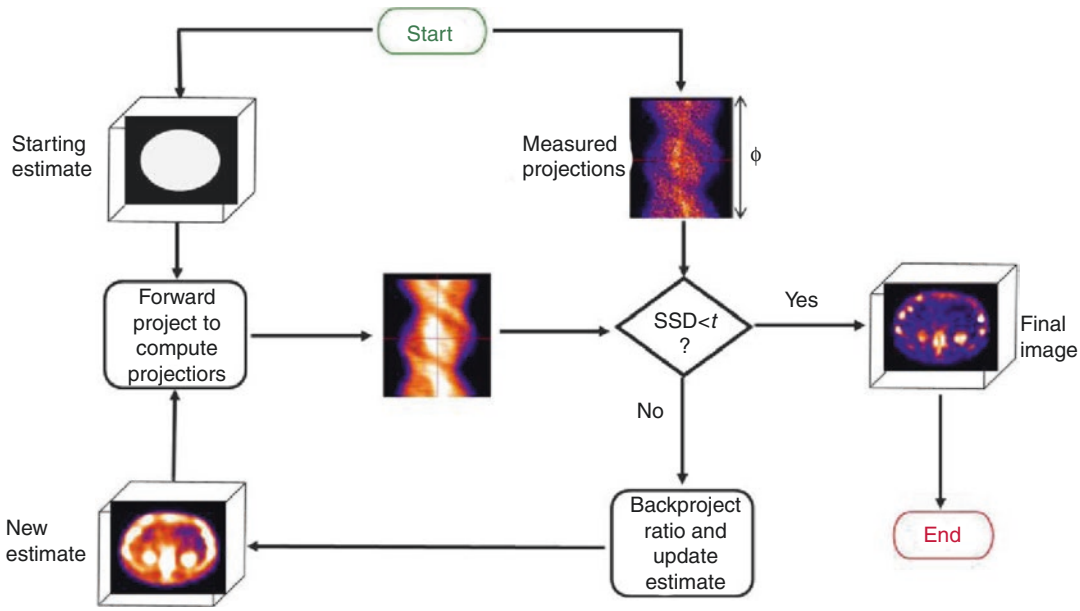

Fig. 1.11 General scheme used in iterative reconstructions is shown. Successive estimates of the reconstruction are updated until a criteria such as sum of squared differences (SSD) between acquired data and estimated reconstruction are below a threshold (t)

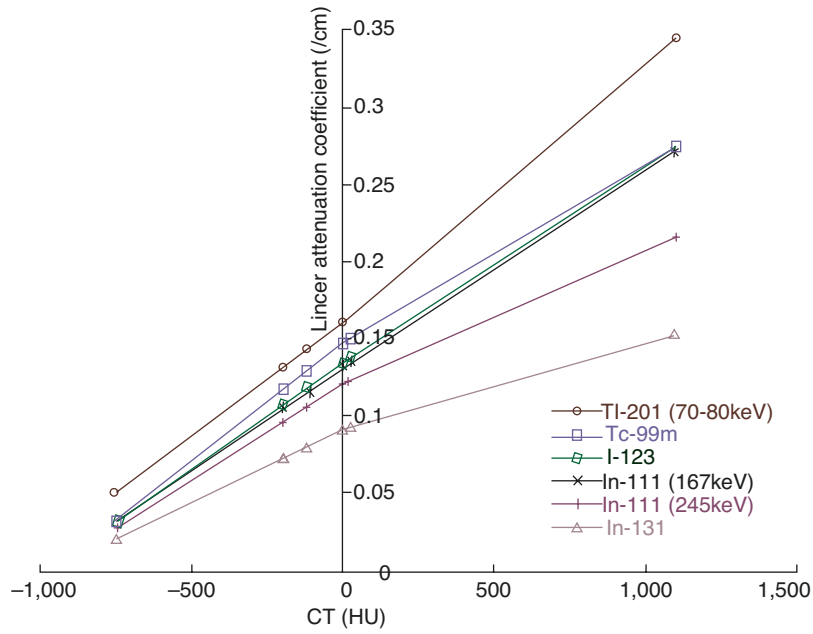

Fig. 1.12 The conversion curves for attenuation coefficients measured experimentally between commonly used radionuclides in SPECT imaging and CT (Hounsfield) numbers are shown for a variety of materials of different density. Note that the bi-linear nature increases with increasing photon energy, as the photon energies move further away from those dominated at low energy by photo-electric interaction

recombine. The majority of the pixels in the image above the threshold tend to be from bony structures only. The process for converting a CT image to an attenuation map is shown in Fig. 1.13.

If the reconstruction algorithm used for the SPECT data is filtered back-projection then CT data can be used in a post-reconstruction correction such as a modification of the Chang method [19] using measured attenuation data rather than assuming a ellipse containing a uniform attenuation coefficient [1]. The correction for photon attenuation can be included in the iterative reconstruction process as the forward-projection/back-projection steps model the image formation process.

Scatter correction can also use the CT data to improve the accuracy of the correction. The main techniques that have been validated for SPECT scatter correction are the energy window-based triple energy window (TEW) method [20], the convolution-based Transmission Dependent Scatter Correction (TDSC) [21], and the direct calculation methods based on the physics of scattering [22, 23]. The latter two methods can both use CT to improve the accuracy of the correction.

1.5.5 Corrections for Resolution

Current generation SPECT reconstruction algorithms based on iterative techniques commonly employ correction for resolution losses by implementing a PSF model at the re-projection step of the iterative algorithm. This effectively creates reconstructed data that is corrected for the effects of the system PSF; however, noise propagation can be an issue, as can artefacts introduced in the reconstructed image, particularly at boundaries of high contrast. The system PSF should ideally be modelled at varying source–to–collimator distances for each radionuclide and collimator.

The poor resolution of SPECT reconstructed data has also been addressed for the specific scenario of bone imaging in the Siemens xSPECT Bone™ algorithm, which makes use of the ordered subset conjugated gradient minimisation (OSCGM) approach. This reconstruction algorithm uses the accompanying CT data which gets segmented into five distinct zones based on HU: air, fat, soft tissue, medullary bone, and cortical bone. The zones are used to inform and enhance the resolution of the reconstructed bone SPECT data, creating SPECT images with sharp foci of uptake in anatomical bone areas (see Fig. 1.14).

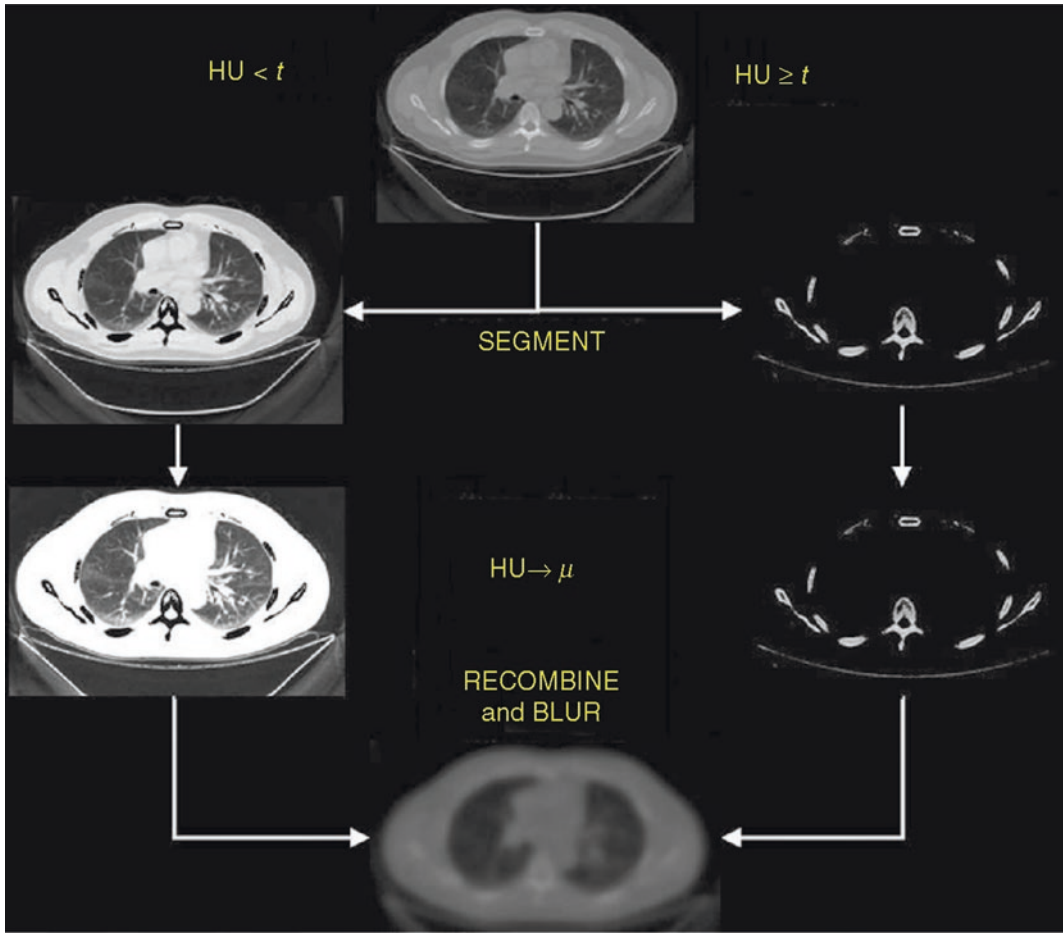

Fig. 1.13 The process to convert a CT image to an attenuation map is shown. The data are firstly classified and segmented based on the point t at which the shape of the bi-linear relationship in Fig. 1.12 between CT number (Hounsfield Unit, HU) and the attenuation coefficients change (usually around 0–50 HU). Each segmented data set is then converted using the appropriate regression equation (the 'HU → μ' step in the figure) and the data are subsequently recombined by adding together and blurred to approximately match the spatial resolution of the SPECT images, so as not to introduce any sharp boundaries or artefacts into the resultant reconstruction

1.6 CT for SPECT/CT

The use of X-rays to produce three-dimensional (3D) anatomical mapping of body density relies on technology analogous to that of SPECT, where computed tomography is performed via reconstruction of a series of one-dimensional (1D) projections acquired throughout 180°. At the most basic level, a single projection image is formed by the detection of X-rays transmitted through the patient, where the changing density or contrast across an image is representative of the differing attenuation properties within the patient due to different tissue thickness and densities that the beam must traverse. Given the loss of information in the dimension parallel to the direction of the beam (the Radon transformation), rotation of the beam and detector arrangement to acquire transmission images through many projection angles allows for the reconstruction of the 2D slice-oriented data.

Generally speaking, X-ray CT image quality is determined by a number of factors, some of which are under the operator's control, others which are governed by the hardware. Table 1.3 summarises the most common factors and their

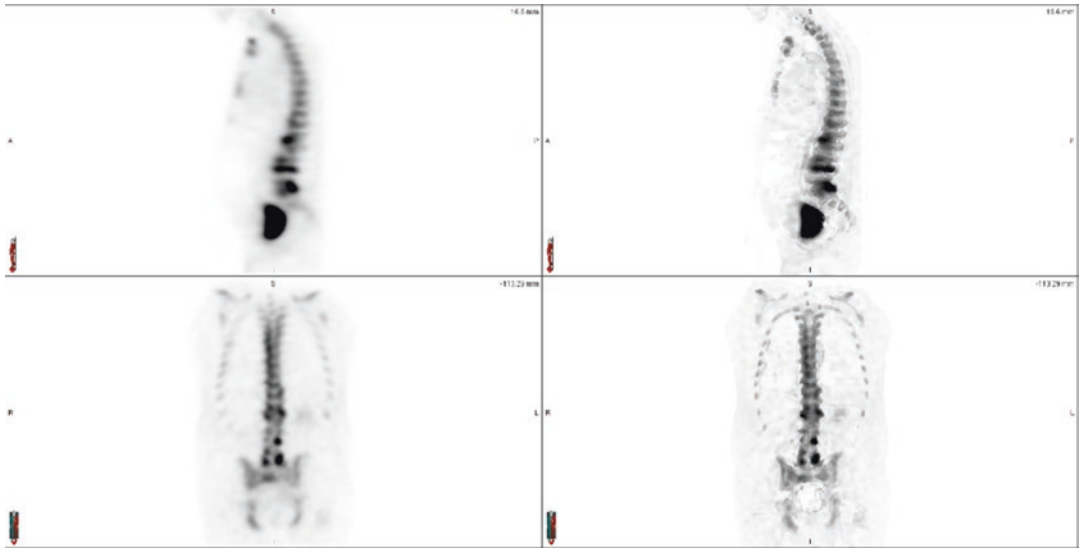

Fig. 1.14 A comparison of the Siemens standard OSEM algorithm (Flash3D) (left) and the skeletal zoning reconstruction (xSPECT Bone) (right) on a two-bed bone SPECT/CT

Table 1.3 Factors affecting CT image quality, related directly to the contrast and spatial resolution of the resulting reconstruction

Contrast resolution (CR)		Dose	Spatial resolution (SR)	
mAs	Increasing the mAs increases the number of photons contributing to the image	$D \propto \frac{SNR^2}{\Delta^3 T}$ Where D is dose, SNR is signal to noise ratio, Δ is the pixel dimension, and T is the slice thickness	Detector spacing and width	Influences sampling – Smaller detectors increase the cut-off (Nyquist) frequency and improve SR
Dose	Dose increases linearly with mAs		Number of projections	Increasing the number of views allows higher spatial frequencies in the image to be displayed without aliasing
Pixel and FoV size	Increasing pixel dimensions to incorporate a larger FoV will increase the photons in each pixel		Pixel and FOV size	The size of the FoV will determine the pixel dimensions for a given reconstruction matrix
Slice thickness	Increasing slice thickness increases the number of photons to produce the image		Slice thickness	Increased slice thickness reduces SR and may blur edges in the transaxial plane
Reconstruction filter	Low pass filters improve CR at the loss of spatial resolution		Reconstruction filter	Kernel shape affects SR – High pass filters give the best SR, at the expense of increasing noise
Patient size	Larger patients attenuate more x-rays, reducing the number of photons and so the signal and CR		Number of rays	Reducing the number of rays is analagous to increased spacing between detectors along an array, and deteriorates SR
Gantry rotation speed	Faster rotation reduces the mAs used to produce each image, reducing CR		Helical pitch	Increasing pitch will deteriorate the SR

impact on image quality, defined by both contrast resolution (CR) and spatial resolution (SR). Improvement of image quality requires a balance of both CR and SR, which must always be considered under the premise of keeping radiation dose as low as reasonably achievable (ALARA). The current (mA) provided to the X-ray source will determine the intensity of the photon flux which is available to contribute to the image, and the tube voltage (kV_p) will determine the energy of the flux and quality of the X-ray beam. A beam of poor quality will result in noisy projection and reconstructed data and will limit the contrast in the image. Beam current and voltage are adjustable parameters which the operator has, to some extent, control over, allowing modification depending on patient thickness and age (to limit dose). Other related factors which the operator has some control over are the size of the FoV and the matrix size or pixel dimensions. For the same FoV, if the pixel size is reduced to improve SR for a given mA and kV_p (same dose), fewer photons will be contributing to the data in each pixel of the image, resulting in a deterioration in the signal to noise ratio (SNR) and CR. As such, the SNR, pixel dimensions, slice thickness, and radiation dose are all related.

The thickness or collimation of the beam itself will depend on whether or not the system is projecting on to a single row of detectors, or a series of multiple rows of detectors, allowing for multiple slices to be acquired simultaneously (see Fig. 1.15). A thicker beam collimation results in a larger volume of the patient being scanned at one time, at the cost of decreased image resolution. Due to the fact that single-slice technology requires a beam that is highly collimated relative to the size of the detector array, a large percentage of X-rays emitted by the tube do not contribute to the image, and only a single slice is acquired for every rotation of the tube. The effective slice thickness is influenced by both the width of the fan beam and the speed of the patient table (helical or spiral CT), or the pitch (the ratio between the distance that the CT table moves during one revolution of the tube to the total collimation). Ideal image quality is reached when the distance the table travels during one revolu-

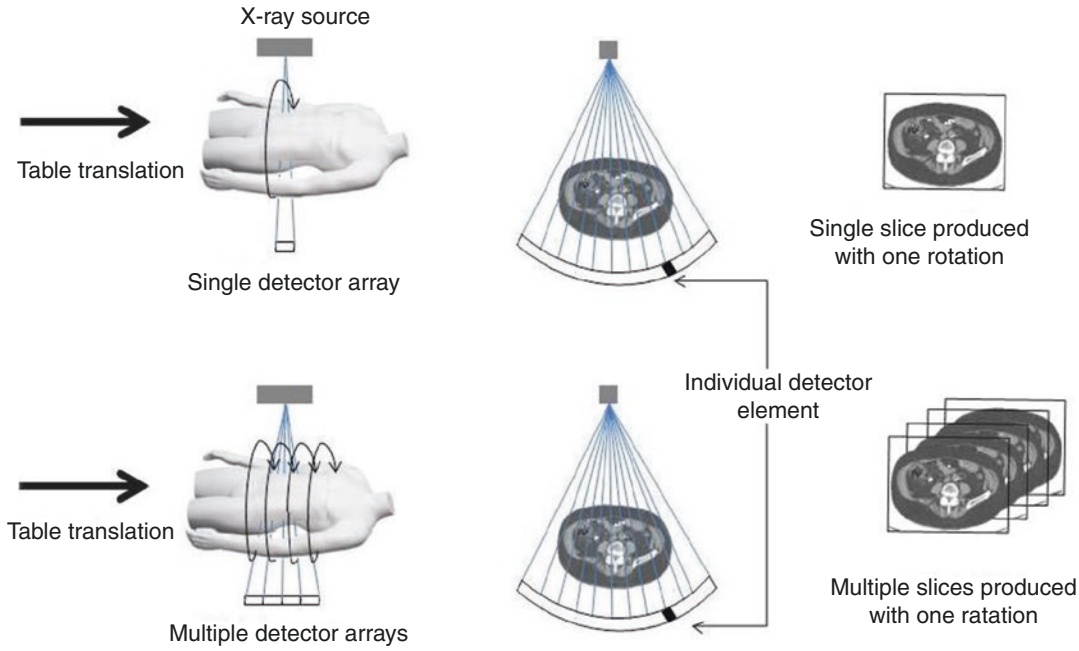

Fig. 1.15 Principles behind single slice and multi slice x-ray CT acquisition. Slice thickness is determined by the collimation of the beam, the detector width and the pitch (related to the speed at which the patient table feeds in to the scanner, and so the 'tightness' of the spiral ray traced by the rotating beam)

tion is equal to the beam collimation or slice thickness. Increasing the pitch will increase volume coverage (and reduce patient dose) but affects image quality. Image quality is also determined by reconstruction parameters, such as filtering, the interpolation algorithm used, and the reconstruction increment, or the degree of overlap between slices, which improves image quality when kept to a minimum at the cost of increased image storage space and computing time.

Alternatively, multi-slice scanners allow for faster image acquisition of the same volume with no compromise on image quality. The effective slice thickness is determined by the number of detector arrays available, the collimation of the beam, and the binning of detector elements. Since the beam is pre-collimated to fall on an entire row of detector arrays, the fan beam extends to a cone-beam geometry, which also has implications for the reconstruction algorithm and requires corrections for beam divergence.

Both the hardware and software components of CT scanners have undergone many developments since the introduction of X-ray CT scanning in the 1970s. In terms of the role of CT scanners in nuclear medicine hybrid imaging, the first commercial SPECT/CT system was introduced in 1999 (GE Discovery VG Hawkeye). This saw the combination of a dual-head SPECT system with a low-powered X-ray CT subsystem, equivalent to a dental tube, operated at 140 kV_p and 2.5 mA. The Discovery Hawkeye employed slip-ring technology for continuous CT acquisition during patient translation through the gantry, with a rotating fan beam from an X-ray tube coupled to a single-curved detector array. The X-ray CT component of the hybrid Hawkeye system was initially single-slice technology, requiring a slow 20 s rotation time and resulting in 2.5 mm in-plane resolution for non-diagnostic quality CT data, however was adequate for the purposes of attenuation correction of the SPECT data and low-resolution anatomical localisation. The Discovery Hawkeye system was updated to the Infinia Hawkeye 4 SPECT/CT with four-slice CT, each of 5 mm thickness, improving axial resolution. It also introduced spiral acquisition which improved (i.e., reduced) total CT scanning time. Such systems offered cost-effective tools for hybrid imaging where diagnostic quality CT was not required and were also favourable in the nuclear medicine community due to their 'low-dose' status and small installation footprint.

Fully diagnostic CT scanners were integrated into commercial hybrid scanners in 2004 in the form of the Siemens Symbia T series and the Philips Precedence, which incorporate dual-head SPECT systems with diagnostic-performance multi-slice CT scanners comparable with conventional CT scanners. The Siemens Symbia T series, available with a 1-, 2-, 6-, or 16-slice CT, uses a diagnostic quality CT operating at up to 130 kVp and 345 mA (T16) with a rotation speed of as little as 0.5 seconds. Both high-end and low-end CT performance components from various generations of SPECT/CT systems can be used for attenuation correction; however, the high-end systems see an improvement in signal-to-noise characteristics in the reconstructed data, and highly detailed anatomical data are available with the multi-slice options due to improved spatial resolution and scan speeds. Current models of scanners that employ up to 64-slice CT in conjunction with SPECT allow for short scan times that are adequate for high-speed studies involving iodinated contrast and coronary angiography studies [24].

An alternative CT technology was introduced to hybrid scanners in 2008 with the launch of the Philips Brightview XCT, which saw a flat panel cone-beam CT component (CBCT) mounted on the same rotatable gantry as the SPECT component, in a co-planar geometry. This co-planar configuration offers the advantage of reduced room size requirements and reduced system weight compared to traditional hybrid systems, and the extended geometry of the flat panel detector along the longitudinal axis has the potential to reduce dose required for a given image quality and volume. The CT component was still relatively slow when compared to conventional CT scanners (minimum rotation time of 12 seconds), and of low power, operating on tube characteristics of 120 kV_p and 80 mA (maximum). The CBCT technology consists of an X-ray source

and flat panel detector mounted on opposite sides of the gantry with a lateral offset such that a single projection covers slightly more than half the CT field of view (FoV). The use of flat panel detectors enables 1 mm isotropic reconstructed voxel size for the entire FoV and can be as small as 0.33 mm isotropic for high-resolution subvolume reconstructions. The different geometry of the CBCT system requires some additional processing steps to be performed at reconstruction. As a result of the lateral offset between the X-ray source and detector, each X-ray projection corresponds to only a half-field projection of the object, resulting in truncation that must be compensated for by combining the projections from the opposite side of the gantry. The combined projections must in turn have a weighting factor applied to correct for the central overlap region. Alternatively, the cone-beam geometry can be accurately modelled in iterative reconstruction algorithms to directly account for the truncation of projection data.

Due to the fact that the primary X-ray beam for the CT component of hybrid systems can produce large amounts of X-ray scatter, significantly higher than that emitted by the radiopharmaceutical used for emission imaging, multimodality systems typically have the imaging planes of the X-ray source and the gamma camera separated by an axial distance of 50 cm or more. The future of SPECT/CT scanners lies in the possibility of truly simultaneous SPECT and CT imaging, with a common detector capable of discriminating between primary emission photons and both scattered photons and the X-ray source, which would require superior temporal and energy resolution [25].

As is the case with standard clinical CT scanning, the CT component of multimodality imaging can suffer from image artefacts. Beam hardening is a phenomenon due to the use of a polychromatic X-ray spectrum. Since X-ray attenuation coefficients are energy dependent, lower energy X-rays will be attenuated more than higher energy X-rays when passing through the same thickness of tissue. As a result, as the beam propagates through the patient, the shape of the spectrum is skewed towards higher energies, and the average energy of the beam becomes increased (or 'harder'). Artefacts are produced in reconstructed CT data due to the fact that different degrees of beam hardening occur at different projection angles, thus rendering the data inconsistent between different projections. Corrections for beam hardening are required during reconstruction of the CT data. Motion artefacts can also be a problem in CT reconstruction and may produce ghosting in the resulting image. The other primary artefact seen in CT reconstruction is partial volume averaging. CT numbers for a given voxel in the reconstructed data are proportional to the attenuation coefficient in the corresponding volume of the patient. If voxels contain only one type of tissue, then this representation is not problematic. However, if multiple tissue types are viewed within a single voxel (such as bone and soft tissue), the CT number is no longer an accurate representation of the corresponding tissue volume, but is instead an average value. Partial volume effects can be reduced with the use of thinner CT slices, and multiple reconstructions at different positions (e.g., 1.25 mm thick and 3 mm thick slices) may be useful.

In addition to CT artefacts, some information on the CT image can potentially result in further artefacts on the reconstructed SPECT data when used for attenuation correction. Attenuation correction artefacts lead to an artificial over- or under-estimate of counts in the reconstructed SPECT data. One common issue arises through the use of contrast media. High-density contrast media may result in erroneously high counts in the corresponding region on the attenuation corrected SPECT data due to the false high-density voxel values on the co-registered CT data used to derive the attenuation correction map. While contrast media exhibits high attenuation and hence signal intensity for low energy X-rays, absorbed by the photo-electric effect, at the higher energies of most γ photon energies, it has an attenuation coefficient close to water. Thus, contrast in a CT scan can lead to erroneously high attenuation coefficients for correcting in SPECT if it is not recognised and scaled separately. Attenuation correction artefacts may be accompanied by streaking in the image and can often be resolved by comparing to the non-attenuation corrected data. Truncation can also be

a potential source of image artefacts. If the SPECT and CT FoV are not the same size, areas of the emission image outside that covered by the CT image will not be corrected for attenuation by the reconstruction algorithm. This often occurs in the 'arms-down' imaging position. Also, misregistration between the two modalities will lead to incorrect compensation in various parts of the reconstructed image, particularly noticeable at boundaries of variable tissue densities, for example, between liver and lung. In terms of cardiac and respiratory motion, even when diagnostic quality CT is used in hybrid systems, SPECT acquisition is of the order of minutes, as opposed to the CT acquisition in seconds or sub-seconds. As such, using the CT data for attenuation correction requires blurring to match the resolution of the SPECT data so as to avoid attenuation correction artefacts.

The radiation dose from the X-ray CT component of hybrid imaging is often seen as a limiting factor in multimodality imaging. Vendors have been continuously striving to reduce radiation dose to patients through improvements in both hardware and software. Certainly, the power of the beam is a big factor when considering patient dose, yet beam intensity and quality must always be balanced against patient size to achieve adequate image quality and signal-to-noise. Faster patient scanning is desirable, yet reducing slice overlap too much can introduce image artefacts. Furthermore, in terms of avoiding respiratory and cardiac motion, if the primary goal of the CT acquisition is for attenuation correction and anatomical localisation, such scan speeds may not be necessary. The major vendors have introduced X-ray CT systems which use automated tube current modulation, such that the beam current is varied during the scan depending on the thickness of the patient at a given slice, as determined by the scout or topogram. Furthermore, the recent introduction of statistical iterative reconstruction of X-ray CT data, as opposed to conventional filtered back-projection, has resulted in a new meaning of the phrase 'low-dose CT'. Iterative algorithms are based on the principle that, unlike FBP, it is not assumed that noise is evenly distributed across the entire image, and it is instead selectively identified and minimised during reconstruction based on a mathematical model. The ability to selectively reduce image noise allows higher quality image data at lower radiation dose compared to FBP to be generated. Dose reductions of the order of 60% are typical, at no cost to temporal or spatial resolution in the reconstructed image [24]. Statistical modelling of the reconstruction process is ideal for incorporating non-standard geometries and corrections; however, it does in turn result in increased computation time due to complex modelling in software. In terms of hybrid scanners in nuclear medicine clinics, this may not be an issue, given that the CT data can be acquired prior to the SPECT study, and reconstruction can take place during the acquisition of emission data.

1.7 Quantitative SPECT/CT

The requirements for producing quantitative data in emission tomography, in general, are: (i) a reconstruction algorithm that behaves in a linear fashion in terms of the reconstructed radioactivity concentration, (ii) an algorithm to compensate for photon absorption within the body, (iii) an algorithm to remove scattered radiation from the data, and (iv) the ability to calibrate the reconstructed data in $kBq.cc^{-1}$. There are several other factors that may influence the quantitative accuracy of reconstructed SPECT data including decreased apparent radioactivity concentration in objects less than approximately three times the spatial resolution of the system and therefore affected by the partial volume effect, count rate losses due to dead time within the instrumentation, radioactive decay during the acquisition process, and corrections and normalisations for spatial and temporal variations in detector response.

Historically, quantification in SPECT has been challenging due to the source-depth dependent nature of attenuation, and the fact that the requirements listed above must be individually determined for each different radionuclide (gamma energy) and can be affected by window width, detector crystal thickness, and collimator choice. For these reasons, much of the quantitative SPECT techniques were first developed in-

house by specialised groups around the world. A number of clinical studies demonstrating in vivo validation of the accuracy of reconstruction in quantitative SPECT using ^{99m}Tc-labelled radiopharmaceuticals have recently appeared [26–28]. The data are presented as radioactivity concentrations (in kBq.cm^{-3}). From this it is straightforward to display the data as SUV units, as is done in PET. Increasingly, other radionuclides are being investigated for quantitative SPECT reconstruction, including ^{111}In, ^{123}I, ^{131}I, ^{177}Lu, ^{186}Re, and ^{201}Tl.

In 2013, quantitative SPECT became available through vendor-based software, initially by Siemens (xSPECT and Broad Quant algorithms) and followed shortly by GE (Q.Metrix software). The current vendor release software can allow for SPECT quantification and the display of data in SUVs, equivalent to that which we see in PET. A range of radionuclide reconstructions are available; however, ^{99m}Tc bone imaging and theranostics applications such as ^{177}Lu-DOTATATE and ^{177}Lu -PSMA imaging for dosimetry estimates have featured prominently in the literature.

For further reading on the clinical applications of SPECT and the potential for quantitative SPECT/CT, the reader is referred to some recent review articles [29–31].

1.8 Radiation Dose from SPECT/ CT

The addition of a CT scan to a conventional SPECT study will increase the total radiation dose to the subject from the procedure. Any increase in the radiation dose must be balanced against the perceived benefit to the subject. However, it is useful to view this increase in dose relative to the dose from the radiopharmaceutical. It is worth remembering that previously in nuclear medicine attempts to better localise foci of uptake of the radiopharmaceutical were often done by augmenting the original scan with a second radiotracer to aid in localisation. For example, adrenal imaging was often augmented with a ^{99m}Tc renal scan to ascertain the likelihood of the focal uptake being intra-adrenal or in a separate mass anatomically separated from the kidney [32]. In this case, very little extra information may be achieved with the second scan, but there is a not insignificant radiation dose associated with the extra procedure. We would argue that an additional CT scan in this example provides a lot more information about the anatomy of the subject for a comparable or lower effective dose of radiation, especially when using Automated Exposure Reduction (AER) on the CT scanner.

Table 1.4 contains estimates of effective dose (ED) from a variety of radiopharmaceutical and CT procedures as they are used routinely in nuclear medicine.

1.9 QC for SPECT/CT

In addition to the quality control (QC) required for performing optimal SPECT studies, SPECT/CT introduces a number of extra procedures necessary to maintain high-quality clinical studies. Principal among these is testing the accuracy of the co-registration between the SPECT and CT data. As the systems are physically distinct, the physical offset between the systems needs to be determined for application when combining the data. The different manufacturers have different approaches to this adjustment, but all systems require validation of the accuracy of the co-registration which should be performed at regular intervals including after any service or maintenance procedure which has the potential to modify the offset.

The QC requirements for quantitative SPECT are still to be developed. These will need to include a regular check of the agreement between the measured dose calibrator readings and reconstructed SPECT values of radioactivity. As there will potentially be a variety of different SPECT radionuclides used, with different photon energies necessitating different collimators, adjustable PHA energy windows, *etc.,* separate calibrations and checking will be required for each. With the co-operation and implementation by the manufacturer of the SPECT/CT systems, many of the required parameters (such as required for scatter correction) could be pre-defined and fixed for a particular radionuclide/collimator/PHA setting. Strict adherence to the predetermined operating conditions and regular vali-

Table 1.4 A comparison of effective dose from CT procedures used in association with SPECT/CT and conventional radiation dose from a variety of radiopharmaceuticals

Procedure	ED (mSv)	Comment and reference
CT head Hawkeye Infinia 4	0.1	Not diagnostic quality – for AC and anatomical localisation only [34]
CT chest Hawkeye Infinia 4	0.9	
CT abdo/pelvis Hawkeye Infinia 4	1.5	
CT head Symbia T6	0.7	Diagnostic quality. Operating at a 130 kV_p with variable tube current 20–345 mAs [35]
CT chest Symbia T6	7.4	
CT abdo/pelvis Symbia T6	6.1–8.6	
Ventilation lung scan with [^{99m}Tc]-DTPA	0.3	Assumes normal clearance from lung [36]
V/Q lung scan	2.5	40 MBq Technegas (no clearance), 200 MBq [^{99m}Tc]-MAA [36]
[^{99m}Tc]-MAG3 for renal localisation (300 MBq)	3.7	Assumes normal renal function [36]
[^{123}I]-mIBG (4 MBq·kg^{-1})	5.8	Assumed 80 kg person [36]
[^{99m}Tc]-MDP bone scan (800 MBq)	4.6	Assumes normal renal clearance [37]
[^{18}F]-FDG PET scan (370 MBq)	7.0	Without CT [37]
[^{99m}Tc]-SestaMIBI (1100 MBq)	9.0	[36]
'Low-dose' FDG PET/CT scan (250–300 MBq and 130 kVp/80 mA with AER[a])	~15	[38]
^{201}Tl brain SPECT (120 MBq)	26.4	[36]
^{67}Ga (400 MBq)	48.0	[36]

[a]AER – Automated Exposure Reduction

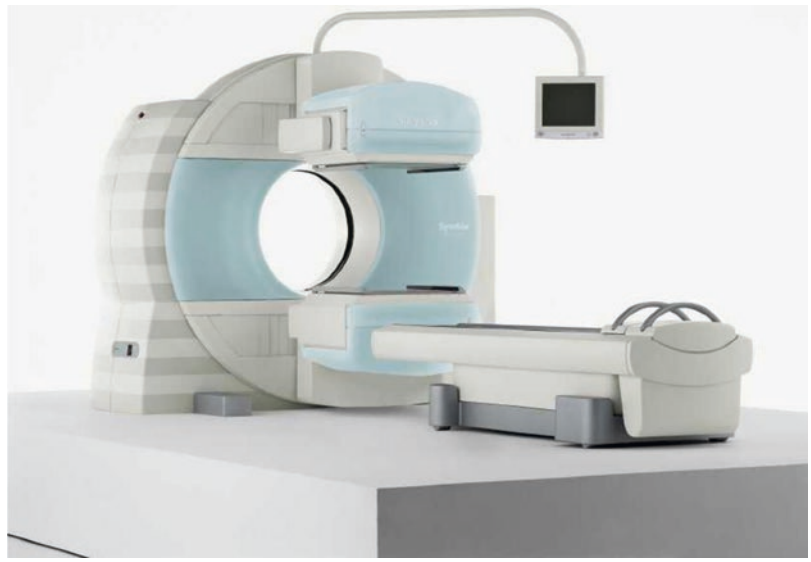

Fig. 1.16 A contemporary SPECT/CT system. The diagnostic quality CT is contained in the large "doughnut" gantry with the two variable angle gamma camera detectors fixed to the front of this (image courtesy of Siemens Healthcare)

dation will be an essential feature when deploying quantitative SPECT.

1.10 Combined SPECT and CT

It is our view that combined SPECT/CT multimodality imaging is a game-changer in terms of the evolution of SPECT for clinical applications. As listed at the beginning of this chapter, there are numerous benefits that the CT data provide both for image interpretation and for improving the quality and accuracy of SPECT images. The near-simultaneous acquisition, in a single imaging session on the same scanning bed, of the emission and transmission (CT) measurements creates the possibility to routinely provide quantitative SPECT data, that is, images reconstructed in units of kBq.cm^{-3}. Clinical applications of this are now being developed. An example of a dual-head SPECT/CT is shown in Fig. 1.16.

References

1. Bailey DL, Hutton BF, Walker PJ. Improved SPECT using simultaneous emission and transmission tomography. J Nucl Med. 1987;28:844–51.
2. Greer KL, Harris CC, Jaszczak RJ, Coleman RE, Hedland LW, Floyd CE, Manglos SH. Transmission computed tomography data acqusiition with a SPECT system. J Nucl Med Tech. 1987;15:53–6.
3. Malko JA, Gullberg GT, Kowalsky WP, Van Heertum RL. A count-based algorithm for attenuation-corrected volume determination using data from an external flood source. J Nucl Med. 1985;26:194–200.
4. Morozumi T, Nakajima M, Ogawa K, Yuta S. Attenuation correction methods using the information of attenuation distribution for single photon emission CT. Med Imag Tech. 1984;2:20–8.
5. Bailey DL. Transmission scanning in emission tomography. Eur J Nucl Med. 1998;25:774–87.
6. Heller G, Links J, Bateman T, Ziffer J, Ficaro E, Cohen M, Hendel R. American Society of Nuclear Cardiology and Society of nuclear medicine joint position statement: attenuation correction of myocardial perfusion SPECT scintigraphy. J Nucl Cardiol. 2004;11:229–30.
7. Moore SC. Attenuation compensation. In: Ell PJ, Holman BL, editors. Computed emission tomography. London: Oxford University Press; 1982.
8. Fleming JS. A technique for using CT images in attenuation correction and quantification in SPECT. Nucl Med Commun. 1989;10:83–97.
9. Hasegawa BH, Gingold EL, Reilly SM, Liew SC, Cann C. Description of a simultaneous emission-transmission CT system. Proc SPIE. 1990:1231.
10. Iwata K, Kwon S-I, Hasegawa BH, Bennett PR, Cirignano L, Shah KS. Description of a prototype combined CT-SPECT system with a single CdZnTe detector. In: IEEE Nuclear science symposium 2000. IEEE; 2000. p. 16/1–5.
11. Tang HR, Brown JK, Da Silva AJ, Matthay KK, Price DC, Huberty JP, Hawkins RA, Hasegawa BH. Implementation of a combined X-ray CT-scintillation camera imaging system for localizing and measuring radionuclide uptake: experiments in phantoms and patients. IEEE Trans Nucl Sci. 1999;46:551–7.
12. Patton JA, Debelke D, Sandler MP. Image fusion using an integrated, dual-head coincidence cameras with X-ray tube-based attenuation maps. J Nucl Med. 2000;41:1364–8.
13. Bailey DL, Roach PJ, Bailey EA, Hewlett J, Keijzers R. Development of a cost-effective modular SPECT/CT scanner. Eur J Nucl Med Mol Imaging. 2007;34:1415–26.
14. Defrise M, Kinahan P, Michel C. Chapter 4. Image reconstruction algorithms in PET. In: Bailey DL, Townsend DW, Valk PE, Maisey MN, editors. Positron emission tomography: basic sciences. London: Springer; 2005.
15. Defrise M, Kinahan PE. Chapter 2. Data acquisition and image reconstruction for 3D PET. In: Bendriem B, Townsend DW, editors. The theory and practice of 3D PET. Dordecht, The Netherlands: Kluwer Academic; 1998.
16. Kinahan P, Defrise M, Clackdoyle R. Chapter 20. Analytical Iimage reconstruction methods. In: Wernick MN, Aarsvold JN, editors. Emission tomography. London: Elsevier Academic Press; 2004.
17. Hudson HM, Larkin RS. Accelerated image reconstruction using ordered subsets of projection data. IEEE Trans Med Imag. 1994;MI-13:601–9.
18. Brown S, Bailey DL, Willowson K, Baldock CA. Investigation of the relationship between linear attenuation coefficients and CT Hounsfield units using radionuclides for SPECT. App Radiat Isot. 2008;66:1206–12.
19. Chang LT. A method for attenuation correction in radionuclide computed tomography. IEEE Trans Nucl Sci. 1978;NS-25:638–43.
20. Ichihara T, Ogawa K, Motomura N, Kubo A, Hashimoto S. Compton scatter compensation using the triple-energy window method for single- and dual-isotope SPECT. J Nucl Med. 1993;34:2216–21.
21. Meikle SR, Hutton BF, Bailey DL. A transmission dependent method for scatter correction in SPECT. J Nucl Med. 1994;35:360–7.
22. Beekman FJ, Kamphuis C, Frey EC. Scatter compensation methods in 3D iterative SPECT reconstruction: a simulation study. Phys Med Biol. 1997;42:1619–32.
23. Kadrmas DJ, Frey EC, Karimi SS, Tsui BM. Fast implementations of reconstruction-based scatter compensation in fully 3D SPECT image reconstruction. Phys Med Biol. 1998;43:857–73.
24. ABADI S, Brook OR, Rispler S, Frenkel A, Engel A, Keidar Z. Hybrid cardiac SPECT/64-slice CTA-derived LV function parameters: correlation and reproducibility assessment. Eur J Radiol. 2010;75:154–8.
25. Seo Y, Mari C, Hasegawa BH. Technological development and advances in single-photon emission computed tomography/computed tomography. Semin Nucl Med. 2008;38:177–98.
26. Willowson K, Bailey DL, Baldock C. Quantitative SPECT using CT-derived corrections. Phys Med Biol. 2008;53:3099–112.
27. Willowson K, Bailey DL, Baldock C. Quantifying lung shunting during planning for radio-embolization. Phys Med Biol. 2011;56:N145–52.
28. Zeintl J, Vija AH, Yahil A, Hornegger J, Kuwert T. Quantitative accuracy of clinical 99mTc SPECT/CT using ordered-subset expectation maximization with 3-dimensional resolution recovery, attenuation, and scatter correction. J Nucl Med. 2010;51:921–8.
29. Bailey DL, Willowson KP. An evidence-based review of quantitative SPECT imaging and potential clinical applications. J Nucl Med. 2013;54:83–9.
30. Mariani G, Bruselli L, Kuwert T, Kim EE, Flotats A, Israel O, Dondi M, Watanabe N. A review on the clin-

ical uses of SPECT/CT. Eur J Nucl Med Mol Imaging. 2010;37:1959–85.
31. Seret A, Nguyen D, Bernard C. Quantitative capabilities of four state-of-the-art SPECT-CT cameras. EJNMMI Res. 2012;2:45.
32. Ong Y-Y, Cohn D, Wijaya J, Roach PJ. The importance of renal localization with MIBG scintigraphy. Clin Nucl Med. 2002;27:479–82.
33. Butler SP, Bailey DL, McLaughlin AF, Khafagi FA, Stephens FO. SPECT evaluation of arterial perfusion in regional chemotherapy. J Nucl Med. 1988;29:593–8.
34. Sawyer LJ, Starritt HC, Hiscock SC, Evans MJ. Effective doses to patients from CT acquisitions on the Ge Infinia Hawkeye: a comparison of calculation methods. Nucl Med Commun. 2008;29:144–9.
35. Larkin AM, Serulle Y, Wagner S, Noz ME, Friedman K. Quantifying the increase in radiation exposure associated with SPECT/CT compared to SPECT alone for routine nuclear medicine examinations. Int J Mol Imaging. 2011;2011:897202.
36. ICRP. ICRP publication 53: radiation dose to patients from radiopharmaceuticals. Ann ICRP. 1988;18
37. Towson JEC. Radiation dosimetry and protection in pet. In: Valk P, Bailey DL, Townsend DW, Maisey MN, editors. Positron emission tomography: basic science and clinical practice. London: Springer-Verlag; 2003.
38. Willowson KP, Bailey EA, Bailey DL. A retrospective evaluation of radiation dose associated with low dose FDG protocols in whole-body PET/CT. Australas Phys Eng Sci Med. 2012;35:49–53.